Correlated polarization-switching kinetics in bulk polycrystalline ferroelectrics. II. Impact of crystalline phase symmetries

R. Khachaturyan* and Y. A. Genenko†
Institut für Materialwissenschaft, Technische Universität Darmstadt, 64287 Darmstadt, Germany

(Received 24 July 2018; published 15 October 2018)

Electric depolarization fields have a great impact on the polarization-switching kinetics in ferroelectrics although they are often neglected in statistical considerations. Analysis of statistical distributions and correlations of polarization and electric field during the field-driven polarization reversal in a bulk polycrystalline ferroelectric by means of the two-dimensional self-consistent mesoscopic switching (SMS) model has revealed that correlations, mediated by electrostatic fields, are mostly isotropic and short range at a typical scale of the mean grain size [Phys. Rev. B **96**, 054113 (2017)]. However, the magnitude of emerging depolarization fields remains substantial and strongly influences the switching kinetics. It is known, on the other hand, that the effect of inhomogeneities, such as a granular structure, on the electric field pattern and local field magnitudes is considerably overestimated in two-dimensional simulations. Three-dimensional extension of the SMS model in the current study allows a realistic evaluation of the impact of spatial correlations on the polarization switching in ferroelectric ceramics and opens a possibility to consider materials of different phase symmetries. It is shown that bound charges at grain boundaries due to mismatching grain polarizations as well as the subsequent depolarization fields are essentially dependent on the crystalline symmetry. This explains great differences in statistical field distributions and polarization kinetics observed in ceramics of different phase symmetries. Field correlations are anisotropic, depend on the material symmetry, but remain in all cases short range at the scale of a grain size. This sheds light on the success of models assuming statistically independent switching of different regions. Evolution of the statistical field distributions in the course of polarization reversal is also symmetry dependent but temporal changes in distributions are not substantial which clarifies a good performance of models neglecting the feedback via depolarization fields.

DOI: 10.1103/PhysRevB.98.134106

I. INTRODUCTION

The most characteristic property of ferroelectrics is their ability to switch the spontaneous polarization when a strong enough electric field is applied. This is a basic process in such ferroelectric applications as digital data storage (FERAM) [1]. Polarization reversal at some location generates a long-range depolarization field [2,3] which should affect the switching process at other locations. However, statistical concepts of polarization reversal typically neglect the feedback effect of depolarization fields and assume independent and uncorrelated nucleation and growth of reversed domains [4–13]. Nevertheless, the nucleation limited switching (NLS) model [7] and the inhomogeneous field mechanism (IFM) model [10,12], assuming a stable statistical distribution of switching times in polycrystalline systems, are able to describe with high accuracy the time-dependent response of ferroelectric ceramics of different chemical compositions and phase symmetries [7,8,12,14–20] as well as of organic ferroelectrics [21–27] and organic-inorganic ferroelectric composites [28,29]. Does it mean that the depolarization fields emerging during the switching process and the interaction of the switching regions can be neglected?

Experimental observations of polarization response by piezoelectric scanning probe microscopy and transmission electron microscopy revealed clustering ranging from a few grains [30] to agglomerations of 10^2–10^3 grains [31,32] in polycrystalline thin films. Similarly, the grain-resolved three-dimensional x-ray diffraction disclosed a collective dynamics in bulk ceramics correlated over approximately 10–20 grains [33–35], a characteristic scale resulting from the complicated and still not understood interplay between the electrostatic and elastic fields. The experimentally revealed characteristic lengths disagree with extremely long-range electrostatic correlations found in phase-field simulations [36] and microscopic modeling [37] of uniform ferroelectric media. Thus, the role of long-range depolarization fields in the switching dynamics of bulk ferroelectric ceramics still remains unclear.

Recent attempts to account for the feedback of depolarization fields in the statistical approach remained mostly within the mean-field approximation assuming the emergence of a time-dependent uniform electric field due to averaging of individual switching events [38–40]. Such an approach still misses the role of local correlations clearly observed in experiment [41–43].

A self-consistent mesoscopic switching (SMS) model [44,45] recently suggested by the authors accounts in a self-consistent way for the local depolarization fields emerging during the field-driven polarization reversal in individual grains of a random polycrystalline medium. This

*rubenftf@gmail.com
†genenko@mm.tu-darmstadt.de

two-dimensional model allowed tracing the evolution of statistical distributions of electric field and polarization as well as their auto- and cross correlations. It was established that both polarization and electric field are correlated at a short range of about the mean grain size. The depolarization fields appeared to be effectively screened by adapting bound charges at grain boundaries. This explains, on the one hand, why the classical statistical approach [6] neglecting correlations may satisfactorily describe total polarization switching at earlier and intermediate stages of polarization reversal in polycrystalline ferroelectrics. On the other hand, the continuously spreading statistical distribution of the local depolarization fields [45] might have a remarkable retarding impact on the later stage of polarization reversal observed in experiment [7,10,13,18,25,27] and modeling [38–40,44]. The question remains open, why the NLS and IFM models neglecting a feedback via depolarization fields are nevertheless able to describe polarization response over the time domain with high accuracy [8,12,14–17].

Two-dimensional (2D) simulations overestimate the effect of obstacles on the field-line pattern [20,46,47] and do not allow consideration of different crystalline symmetries typical of perovskite ferroelectrics which apparently have a great impact on the polarization-switching dynamics [15–17]. Therefore in the current study we extend the SMS model to a three-dimensional (3D) geometry. The paper is organized as follows. An analytical 3D model of a fully polarized uncorrelated ceramic is introduced in Sec. II and serves as a reference limiting case for the following simulations. Analytical calculations of the surface bound charges in uncorrelated ceramics of different symmetries are performed for comparison with the respective correlated cases. A numerical 3D-SMS model is introduced in Sec. III. Simulations within this model presented and discussed in Sec. IV show the time development of the total polarization, statistical field distributions, and spatial correlations of electric field and polarization components during their evolution in the course of the polarization reversal. The results are concluded in Sec. V.

II. ANALYTICAL MODEL OF A FULLY POLARIZED, UNCORRELATED BULK FERROELECTRIC CERAMIC

Ferroelectric ceramics are characterized by random shape of grains and random orientation of the crystal lattice inside the grains. In the current study we focus on the latter factor of randomness which allows one to capture the main reasons for emerging and development of depolarization fields. To this end we use an original model of a ferroelectric ceramic introduced in Ref. [48]. We imagine a sample consisting of a regular cubic lattice of equal tightly contacting single-crystalline cubic grains of size R much larger than the lattice constant of the material. The grain edges are supposed to be aligned along the axes of the Cartesian coordinate system x, y, z as is shown in Fig. 1. The sample of a macroscopic size $L \gg R$ is sandwiched between two plane electrodes located at $z = \pm L/2$. It is supposed to be polarized in a dc electric field substantially higher than the coercive field to the maximum possible spontaneous polarization in the z direction. After that the voltage at the electrodes is set back to zero so that the remanent polarization $\mathbf{P}_r$ in the z direction remains. This state will be considered as an initial one for the polarization reversal investigated in the next section.

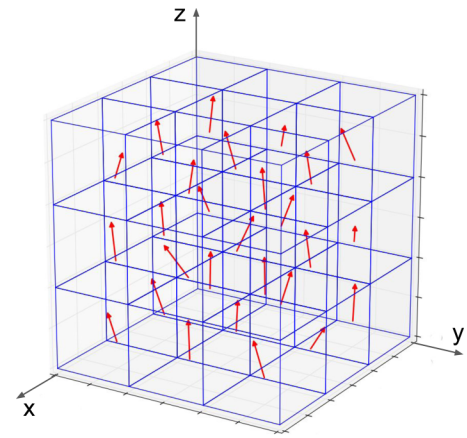

FIG. 1. Scheme of a three-dimensional distribution of polarization in a fully polarized ferroelectric ceramic represented by a regular array of cubic grains with arbitrary crystalline orientations.

Since the crystal structure of the grains is formed at temperatures far above the ferroelectric phase transition, the crystal axes orientation in different grains is supposed to be arbitrary and not correlated. In the high electric field the spontaneous polarization in each grain $\mathbf{P}_s$ takes on the direction of one of the pseudocubic symmetry axes closest to the direction of the applied field (see Fig. 1). Accordingly, an anisotropic dielectric permittivity tensor is arbitrarily oriented in the grains with its c axis along the local spontaneous polarization. The vectors $\mathbf{P}_s$, assumed to be uniform within each grain, have the same magnitude of P_s and are statistically distributed within the cone defined by the polar angle $\theta < \theta_{\max}$ with respect to the z axis. The angle $\theta_{\max}$ depends on the phase symmetry of the ferroelectric. For the cases of the tetragonal (T) and rhombohedral (R) symmetries the respective angles $\theta_{\max,t}$ and $\theta_{\max,r}$ were found by Uchida and Ikeda [49] to be equal to each other and amount to $\arcsin\sqrt{2/3}$. In the orthorhombic (O) phase this angle equals $\theta_{\max,o} = \pi/4$.

In the rest of this section, spatial fluctuations of the bound charges at the grain boundaries in the highly poled state of ceramics of different phase symmetries will be evaluated. For their calculation one needs a procedure of statistical averaging which is specified as follows.

A. Configurational averaging

Configurational averaging of local angle-dependent variables over the ensemble of all possible random configurations, which is equal to the averaging over the infinite sample volume, may be performed using the distribution function $f(\theta, \varphi)$ of a possible polarization directions compatible with the applied field direction. Derivation of this function presents a nontrivial task involving cumbersome calculations. For the case of tetragonal symmetry, the appropriate distribution function $f_t(\theta, \varphi)$ was derived in Ref. [48]:

$$f_t(\theta,\varphi) = \begin{cases} \frac{3}{2\pi}, & 0 \leqslant \theta \leqslant \frac{\pi}{4}, \\ \frac{6}{\pi^2}\left[\frac{\pi}{4} - \arccos\left(\cot\theta\right)\right], & \frac{\pi}{4} \leqslant \theta \leqslant \theta_{\max,t}, \end{cases} \tag{1}$$

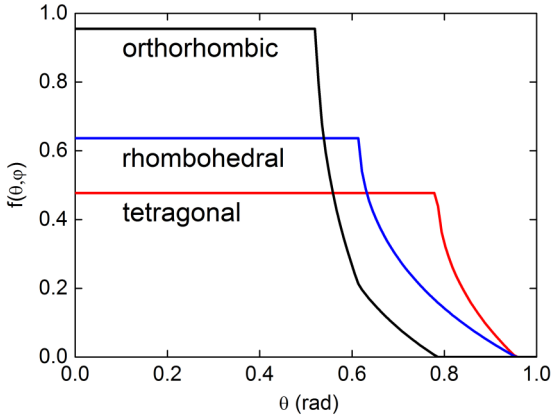

FIG. 2. Two-dimensional projection of statistical distributions $f(\theta, \varphi)$ of polarization directions on an arbitrary φ plane in fully polarized uncorrelated ferroelectric ceramics of different phase symmetries.

for $0 \leqslant \varphi < 2\pi$ where φ and θ are, respectively, the azimuthal and polar angle in spherical coordinates associated with the above introduced cartesian coordinates and centered in the center of the chosen grain. The distribution functions $f_r(\theta, \varphi)$ and $f_o(\theta, \varphi)$ for the cases of rhombohedral and orthorhombic symmetries are derived in Appendixes A and B and given by Eqs. (A5) and (B5), respectively. Since the considered poled polycrystalline ferroelectrics belong to the Curie symmetry group ∞m [50], the distribution functions are independent of the azimuthal angle and can be presented on a plane graph [51] as is shown in Fig. 2. It is seen that the orthorhombic phase, possessing twelve possible stable polarization directions, is described by the most concentrated polarization distribution $f_o(\theta, \varphi)$, followed by the wider rhombohedral distribution $f_r(\theta, \varphi)$, related to eight possible polarization directions, and the most spread tetragonal distribution $f_t(\theta, \varphi)$, related to six possible polarization directions.

Let us introduce as in Ref. [48] a three-dimensional numeration (integer coordinates) of grains $[n, k, m]$ associated with the Cartesian coordinates so that the centers of the grains take positions (nR, kR, mR). For evaluation of macroscopic mean values the sample will be considered as an infinite one so that the numbers $[n, k, m]$ run over all integers from $-\infty$ to $+\infty$. Assuming statistical independence of random angle variables in different grains the distribution function for polarization directions in all grains reads

$$F(\{\theta_i, \varphi_i\}) = \prod_{n,k,m} f(\theta_{n,k,m}, \varphi_{n,k,m}), \tag{2}$$

where $\{\theta_i, \varphi_i\}$ denotes the manifold of spherical angles in all grains, while $\theta_{n,k,m}$ and $\varphi_{n,k,m}$ denote the angles in the grain with numbers $[n, k, m]$. Calculating an ensemble average of a quantity $g(\{\theta_i, \varphi_i\})$,

$$\langle g \rangle = \prod_i \int \sin(\theta_i) d\theta_i \int d\varphi_i \, g(\{\theta_i, \varphi_i\}) F(\{\theta_i, \varphi_i\}), \tag{3}$$

one should take into account that all azimuthal and polar angle variables change in the same angle ranges, $0 \leqslant \varphi < 2\pi$, $0 \leqslant \theta \leqslant \theta_{\max}$. Thus, the ensemble average of the polarization along the z-axis $\langle P_z \rangle$ is reduced to

$$P_r = P_s \langle \cos(\theta_{n,k,m}) \rangle = P_s \int_0^{2\pi} d\varphi_{n,k,m} \times \int_0^{\theta_{\max}} f(\theta_{n,k,m}, \varphi_{n,k,m}) \sin(\theta_{n,k,m}) \times \cos(\theta_{n,k,m}) d\theta_{n,k,m}. \tag{4}$$

By applying the respective distribution functions for ceramics of different phase symmetries this formula brings about the maximum possible values of polarization $P_{\max}$ in nontextured ceramics of tetragonal, rhombohedral, and orthorhombic symmetries presented in Table I which coincide with the numbers known in literature [49,52,53]. The perpendicular x component of polarization in all cases vanishes,

$$\langle P_x \rangle = P_s \langle \cos(\theta_{n,k,m}) \cos(\varphi_{n,k,m}) \rangle = 0, \tag{5}$$

as well as $\langle P_y \rangle = 0$ for symmetry reasons. Finally, the local polarization can be conveniently decomposed in a sum of the mean and fluctuation polarizations as $\mathbf{P}_s = \mathbf{P}_r + \Delta\mathbf{P}_s$, where $\langle \mathbf{P}_r \rangle = (0, 0, P_{\max})$ with $\langle \Delta\mathbf{P}_s \rangle = 0$.

TABLE I. Mean polarization values and variances of bound charge densities at grain boundaries in uncorrelated tetragonal (T), rhombohedral (R), and orthorhombic (O) ceramics.

	T	R	O
$P_{\max}/P_s$	0.831	0.866	0.912
$\mathrm{SD}(\sigma^x)/P_s$	0.547	0.492	0.406
$\mathrm{SD}(\sigma^z)/P_s$	0.141	0.126	0.080

B. Variances of bound charges at grain boundaries

Surface bound charge densities at the faces of a cubic grain with the number $[n, k, m]$ located inside the bulk material are constant over the cubic faces and result from discontinuities of the respective normal components of the polarization $\Delta\mathbf{P}_s$ in the neighbor grains. Namely, the charge density at the bottom face perpendicular to the axis z equals

$$\sigma^z_{n,k,m} = P_s[\cos(\theta_{n,k,m-1}) - \cos(\theta_{n,k,m})], \tag{6}$$

the charge density at the left face perpendicular to the axis x equals

$$\sigma^x_{n,k,m} = P_s[\sin(\theta_{n-1,k,m}) \cos(\varphi_{n-1,k,m}) - \sin(\theta_{n,k,m}) \cos(\varphi_{n,k,m})], \tag{7}$$

and the charge density at the left face perpendicular to the axis y equals

$$\sigma^y_{n,k,m} = P_s[\sin(\theta_{n,k-1,m}) \sin(\varphi_{n,k-1,m}) - \sin(\theta_{n,k,m}) \sin(\varphi_{n,k,m})]. \tag{8}$$

Configurational averaging of the above charge densities for internal grains with the distribution functions $f(\theta_{n,k,m}, \varphi_{n,k,m})$, equal to the averaging over the sample volume, results in vanishing mean values $\langle \sigma^{x,y,z}_{n,k,m} \rangle = 0$, which does not preclude the fact that local values (6)–(8) in a certain random system are finite. For the top plane of a physical sample, Eq. (6) is not valid because there are no grains above

the top grain layer. For that reason the nonzero mean value $\langle\sigma^z_{n,k,m}\rangle = P_r$ produced by the mean polarization $\mathbf{P}_r$ prevails at the top plane of the sample $z = L/2$. Similarly, $\langle\sigma^z_{n,k,m}\rangle = -P_r$ at the bottom plane of the sample $z = -L/2$.

Typical magnitudes of the local charge densities at the internal grain faces (6)–(8) are characterized by the standard deviations (SD) of the respective charge densities,

$$\mathrm{SD}(\sigma^x) = \sqrt{\left\langle\left(\sigma^x_{n,k,m}\right)^2\right\rangle} = \mathrm{SD}(\sigma^y) \quad \text{and}$$
$$\mathrm{SD}(\sigma^z) = \sqrt{\left\langle\left(\sigma^z_{n,k,m}\right)^2\right\rangle}. \tag{9}$$

Table I shows their values normalized to P_s for ferroelectric ceramics of different phase symmetries. Details of calculations are presented in Appendix C. Substantial differences between $\mathrm{SD}(\sigma^z)$ and $\mathrm{SD}(\sigma^x)$ are explained by the fact that the polarization direction in the (x, y) plane and, hence, the variation of its azimuthal angle are not restricted while the polar angle is confined to the cone $\theta \leqslant \theta_{\max}$ around the positive z direction.

III. 3D SELF-CONSISTENT MODEL OF POLARIZATION-SWITCHING KINETICS IN A BULK FERROELECTRIC CERAMIC

The main task of the current study is to account for the electric interaction between different switching regions due to the emerging depolarization fields and finally to evaluate the feedback effect of these fields on the global polarization kinetics. To this end we advance here a three-dimensional self-consistent mesoscopic switching model (3D-SMS) of polarization reversal kinetics in a bulk ferroelectric ceramic which conceptually extends the previously developed 2D-SMS model [45]. Differently from the latter, the 3D-SMS model does not assume a random grain structure of the material but uses instead the regular cubic grain structure with randomized crystal lattice orientations delineated in Sec. II. Similarly to the previous 2D approach, the 3D-SMS model combines a numerical solution of the coarse-grained local equations for polarization development in individual grains with the global calculation of the electric field by the finite-element method (FEM), the whole algorithm being realized within a FlexPDE program (PDE Solutions Inc.). In the following, the description of ferroelectric ceramics and the evolution equations are presented in detail.

A. Creation of a random structure

We consider a polycrystalline bulk ferroelectric placed between two—top and bottom—plain electrodes. A cubic sample is assumed to consist of equal cubic single-crystalline grains as is schematically shown in Fig. 1. Each grain possesses the same phase symmetry—tetragonal, rhombohedral, or orthorhombic—and a random crystal orientation uncorrelated with neighbor grains. An initial polarization state is assumed to be created by a very strong electric field applied in positive z direction given by the vertical axis in Fig. 1. In this case, polarization directions in individual grains are arbitrarily chosen from an appropriate three-dimensional angle distribution function for a nontextured ferroelectric bulk ceramic of the respective symmetry using Eq. (1) or (A5) or (B5). According to the chosen polarization (c-axis) direction (and a random rotation around it), each grain is characterized by a dielectric tensor ε_{ij}, with principal values of the relative permittivity taken from Refs. [54–57] for exemplary materials of different symmetries.

In a coarse-grained consideration, polarization within each grain is characterized by a mean value $\mathbf{p}_i$ approximately presenting a multidomain state that entails discontinuities at grain boundaries where surface charge densities arise, equal to an abrupt variation of the normal component of the polarization when traversing the boundary. The electric field, in contrast, varies within the grains according to the Laplace equation and natural boundary conditions at the grain boundaries which comprise continuity of the tangential electric field and discontinuity of the normal component of the electric displacement equal to the surface charge density. To apply an external electric field of either sign in z direction, the top and the bottom surfaces of the computation box are held at constant potentials, whereas periodic boundary conditions are applied in x and y directions.

B. Evolution equations

The change in the polarization of individual grains will be considered in the spirit of the Kolmogorov-Avrami-Ishibashi (KAI) model of domain nucleation and growth [4–6] giving the total polarization reversal as

$$\Delta p(t) = 2P_s\{1 - \exp[-(t/\tau)^\beta]\}, \tag{10}$$

where P_s is the saturation polarization, β is the Avrami index depending on the reversal domain dimensionality, t is the time elapsed after the voltage application, and τ is the characteristic switching time. It is well known that τ is strongly dependent on the electric field value E, for example, according to the empiric Merz law [58] $\tau(E) = \tau_0 \exp(E_a/E)$, where E_a is the so called activation field and τ_0 is the switching time at very high fields.

In the original KAI approach the field E is assumed to be uniform in the whole system and constant in time. In ferroelectric ceramics the field is indeed distributed nonuniformly due to complying with the boundary conditions at the grain boundaries. In the spirit of the IFM model [10,12] we suppose that the local switching time $\tau(E)$ is determined by the local value of the electric field [59]. In accordance with our coarse-grained consideration, for the local field E the mean-field value over each grain will be taken. Over and above, we account for the fact that local switching time values are also time dependent together with the field E. To be able to capture this dependence we substitute the global time dependence of the polarization, Eq. (10), by the instantaneous rate of the polarization change derived by differentiation of Eq. (10) with respect to the time t:

$$\frac{dp}{dt} = \frac{P_s\,\mathrm{sgn}(E) - p}{\tau}\beta\left(\frac{t}{\tau}\right)^{\beta-1}. \tag{11}$$

Here the signum function $\mathrm{sgn}(\cdot)$ determines the direction to which the saturation of the polarization proceeds. This one-dimensional equation should be generalized to the actual 3D case. In the following we assume, as in the classical KAI approach [6], the polarization reversal to be dominated by

180°-switching events (which is generally not true [60–62]), so that the polarization only changes along the randomly chosen c direction within each grain given by a unit vector $\mathbf{n}_i$. This means that the local dielectric tensor remains unchanged during this process. Thus Eq. (11) can be generalized to the local vectorial form

$$\frac{d\mathbf{p}_i}{dt} = \frac{\mathbf{n}_i P_s \,\mathrm{sgn}(\langle\mathbf{E}\rangle_i \cdot \mathbf{n}_i) - \mathbf{p}_i}{\tau(|\langle\mathbf{E}\rangle_i \cdot \mathbf{n}_i|)} \beta \left[\frac{t}{\tau(|\langle\mathbf{E}\rangle_i \cdot \mathbf{n}_i|)}\right]^{\beta-1}, \quad (12)$$

where $\langle\mathbf{E}\rangle_i$ is the electric field averaged over the volume of the considered grain. Equation (12) takes into account that only the field projection on the local c axis promotes switching.

Calculated local values of the depolarization field ΔE_d scale with the magnitude of the saturation polarization P_s. Typical magnitudes of the field components, estimated exemplarily for lead zirconate titanate (PZT) [48], appear to be of the order of the thermodynamic coercive field which is known to exceed experimentally observed values of the coercive field by few orders of the magnitude [63]. In fact, local electric fields are strongly reduced by various physical mechanisms, first of all, by domain formation [63] and semiconductor properties of ferroelectric materials [64–66]. For low total polarizations, high local fields can be depressed by splitting in domains which leads to lower mean polarizations of grains and accordingly lower bound charges at grain boundaries. At higher polarizations, too high local fields may be depressed by screening of bound charges due to semiconductor effects including band bending and accumulation of charged defects in surface states at grain boundaries. Indeed, the fluctuation field ΔE_d provides a variation of the electrostatic potential across a grain about $\Delta\varphi \simeq \Delta E_d R$ that can reach several tens of volts [48]. Being much larger than a typical band gap in ferroelectric perovskites E_g of 3–4 eV such a potential sweep causes strong band bending and produces electron and/or hole spatial pockets which effectively reduce bound charges at grain boundaries. Due to this internal screening effect the local fields cannot exceed a typical value of $E_g/2qR$, with the elementary charge q, so that the potential sweep remains below $E_g/2q$ [65,66]. The local fields may be further reduced by accumulation of charge defects compensating bound charges at grain boundaries [67].

To account for the internal screening, an effective value of the local saturation polarization $P_s^* = 0.01$ C/m^2 was used for calculation of depolarization fields in the 2D-SMS model [45] that reduced local fluctuation fields to a typical magnitude of the coercive field in tetragonal PZTs. The drawback of this approach is that it uniformly depresses depolarization fields all over the system including locations where the field is already small. This might affect the statistical distribution of local electric fields and distort the true picture of field correlations. For that reason, in the actual 3D-SMS model we introduce another approach. Namely, each time after the FEM calculation of the electric field we apply a criterion testing the local field magnitude E and reducing it to the cutoff field $E_{\mathrm{cf}} < E_g/2qR$ if $E > E_{\mathrm{cf}}$. Thus the depolarization field is only depressed at locations where it is too large. Since the value E_{cf} may result from a sophisticated interplay of the above mentioned physical mechanisms it is used as a fitting parameter when comparing simulations with available data on polarization-switching kinetics.

C. Simulation procedure

Simulations include the following steps:

(1) Generation of a regular 3D array of $10\times10\times10$ cubic grains of size $R = 1$ μm and assigning to each grain a polarization direction (c axis) arbitrarily chosen from the statistical polarization distribution of the appropriate symmetry.

(2) Assignment of material parameters: saturation polarization, activation and cutoff fields, high-field switching time, Avrami index, eigenvalues of the permittivity tensor; assignment of the dielectric permittivity tensor in each grain by arbitrary rotation around its c axis.

(3) Evaluation of the spatial field distribution and average field magnitudes inside each grain using the finite element software FlexPDE.

(4) Evaluation of the polarization change in each grain during the time step Δt by integration of Eq. (12) over Δt using the software FlexPDE for the above calculated local average field values; consequent updating of the polarization in each grain.

(5) Calculation of the total polarization by adding up the local modified polarizations.

(6) Repetition of steps 3–5 until the total polarization reaches a saturated value.

For exemplary tetragonal and rhombohedral systems, lead zirconate titanate ceramics $Pb(Zr_xTi_{1-x})O_3$ with, respectively, $x = 0.515$ and $x = 0.6$ were chosen. The appropriate permittivity values were taken from Refs. [54,55], the other parameters were used as trial values and found by best fitting to the available polarization kinetics data for these compounds [16] as is shown below in Fig. 3. As an example of an orthorhombic ferroelectric at room temperature, potassium niobate $KNbO_3$ was chosen whose polarization and coercive field were taken from Ref. [68] and permittivity tensor from Refs. [56,57]. Sufficient polarization kinetics data for this material are not available, so that the respective kinetic parameters were exemplarily taken over from the solid solution $(1-x)Ba(Zr_{0.2}Ti_{0.8})O_3$-$x(Ba_{0.7}Ca_{0.3})TiO_3$ with $x = 0.5$, which possesses a comparable coercive field [17].

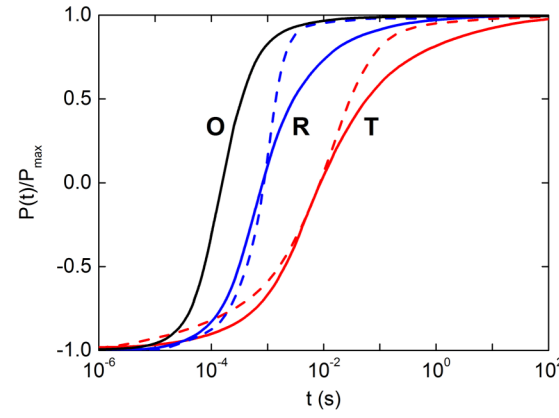

FIG. 3. Time evolution of the total polarization $P = \langle p_z\rangle$ normalized to its maximum value for materials of tetragonal (T), rhombohedral (R), and orthorhombic (O) symmetries, as indicated in the plot, at applied field values 1.8, 1.4, and 0.5 kV/mm, respectively. Solid and dashed lines show, respectively, simulated and experimental response. The other parameters used are gathered in Table II.

TABLE II. E_a, E_{cf}, β, and τ_0 values in tetragonal (T), rhombohedral (R), and orthorhombic (O) ceramics.

	T	R	O
E_a (kV/mm)	35	28	8
E_{cf} (kV/mm)	0.4	0.25	0.1
β	2	3	3
τ_0 (ps)	11.5	1.7	5
ε_{11}	1721	529	160
ε_{22}	1721	529	1000
ε_{33}	382	295	55

IV. SIMULATION RESULTS

A. Polarization-time dependencies

Polarization-time curves obtained from experimental measurements (dashed lines) and calculated ones (solid lines) are presented exemplarily in Fig. 3 for the above introduced materials of tetragonal, rhombohedral, and orthorhombic symmetries at different applied field values. They cannot be displayed on the same graph for the same applied field because the switching processes evolve at very different timescales. Note that the presented processes do not start from the initial highly polarized state described in Sec. II. This fully uncorrelated state includes, among others, unphysical local polarization configurations with highly charged grain boundaries. Due to resulting high local fields such places disappear after few polarization-switching cycles. After that polarization-switching curve becomes completely reproducible and weakly dependent on the applied field direction, a consequence of a finite size of the computation box.

Calculated polarization response demonstrates fair agreement with available experimental data for tetragonal and rhombohedral PZT ceramics using parameter values shown in Table II. The band gap E_g in PZT is known to be about 3.5 eV. The fitting value for the cutoff field E_{cf} is four times smaller than $E_g/2q$. This reveals that the band bending is not of crucial importance in the field suppression mechanism. Another physical reasons could be domain formation, inhomogeneous polarization distribution within domains, and possible non-180° rotations of polarization which are not taken into account in the actual model.

Non-180° rotations play an important role in polarization reversal [60–62] and seem to present a dominating mechanism at the beginning of this process because of much shorter switching times [13,60,69]. They also prevail with decreasing of the applied field value [13] that is supposed to explain the emerging deviation of simulated curves from experimental ones when the field is decreased, as is apparent in Fig. 4 presenting exemplary simulations for tetragonal symmetry. In the following we will use the parameters from Table II obtained by fitting of the kinetic polarization data in Fig. 3 for analysis of spatial fluctuations and correlations of polarization and field.

B. Charge and field spatial fluctuations

A rough insight into the coherence of polarization processes may be gained by studying grain boundary charges,

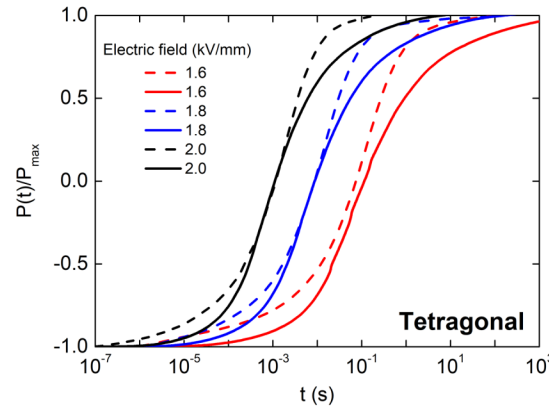

FIG. 4. Polarization-time curves for the tetragonal material at different applied field values as indicated in the plot. Dashed and solid lines show, respectively, experimental data from Ref. [16] and corresponding simulated response.

formed by polarization discontinuities between neighbor grains, in the course of the global polarization reversal. Their mean values averaged over the system volume remain, of course, equal to zero but their typical local magnitudes may be estimated from their variances. First a structure with maximum polarization in each grain is produced to compare standard deviations of simulated surface charges with analytical results of Sec. II B. A good agreement between the former and the latter for both x and z faces of cubic grains was found for all symmetries considered (cf. Tables I and III).

Surface charges vary with the evolution of the total polarization as is shown in Fig. 5. At the beginning of the displayed polarization reversal simulation the system is already somewhat aligned after a few polarization cycles, therefore initial levels of surface charges do not exactly coincide with those of fully uncorrelated systems.

For all phase symmetries, the initial and final polarization states are the most z aligned, exhibiting the lowest level of σ_z spatial fluctuations. At the same time the σ_x fluctuations are at the highest level in these states. Charge fluctuations interchange their intensities in the middle of polarization reversal, exhibiting the highest σ_z and the lowest σ_x spatial fluctuations for intermediate P values. For all phase symmetries the mean level of σ_x fluctuations during the polarization reversal is higher than of σ_z fluctuations, because of unbound polarization directions in (x, y) plane, with the highest difference between them in the most anisotropic tetragonal system [Fig. 5(a)]. Interestingly, the lowest level of charge fluctuations is observed not in the least anisotropic rhombohedral

TABLE III. Simulated maximum polarizations and standard deviations of surface charge densities (both evaluated with inaccuracy of 2%) in uncorrelated tetragonal (T), rhombohedral (R), and orthorhombic (O) ceramics.

	T	R	O
P_{max}/P_s	0.830	0.867	0.911
$SD(\sigma^x)/P_s$	0.541	0.515	0.437
$SD(\sigma^z)/P_s$	0.140	0.119	0.082

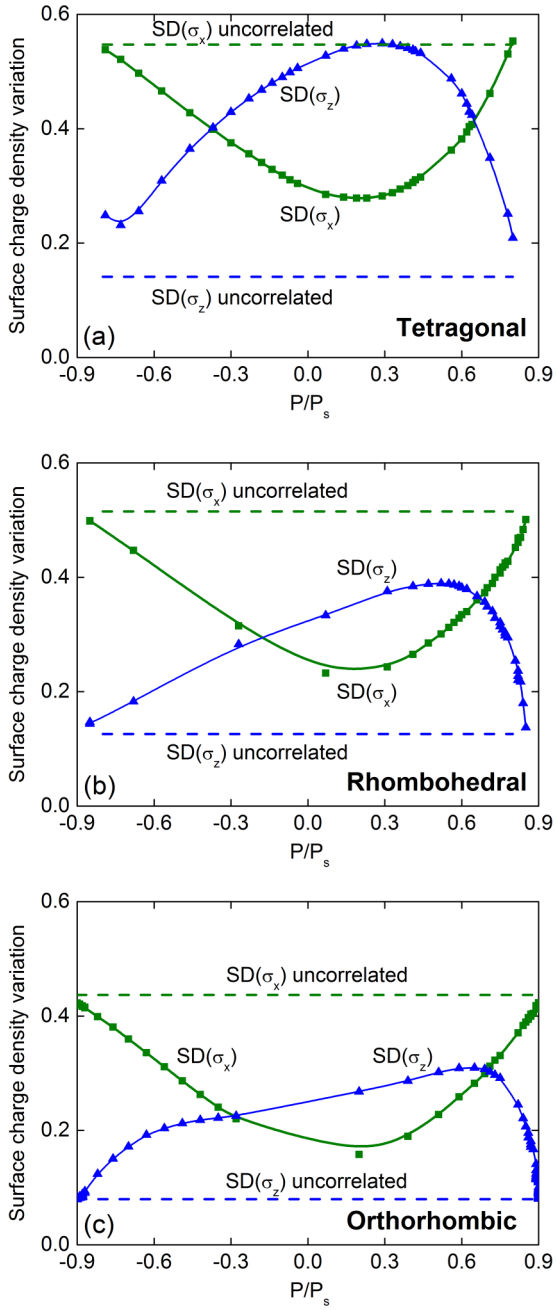

FIG. 5. Evolution of spatial charge fluctuations presented by standard deviations in units of P_s during the polarization reversal in (a) tetragonal, (b) rhombohedral, and (c) orthorhombic systems. Symbols show calculated quantities, solid lines are guide for the eye.

phase [Fig. 5(b)] but in the orthorhombic phase [Fig. 5(c)], obviously thanks to the most focused statistical distribution of polarization axes $f_o(\theta, \phi)$ in the latter phase (see Fig. 2).

Evolution of the field component fluctuations with the development of the total polarization is shown in Fig. 6 exhibiting the highest level of fluctuations in the most anisotropic tetragonal system and the lowest level of fluctuations again in the orthorhombic system. Since the local field components result to the same extent from both σ_x and σ_z charges and these vary with polarization in a complementary way (see Fig. 5) the field fluctuations do not vary much

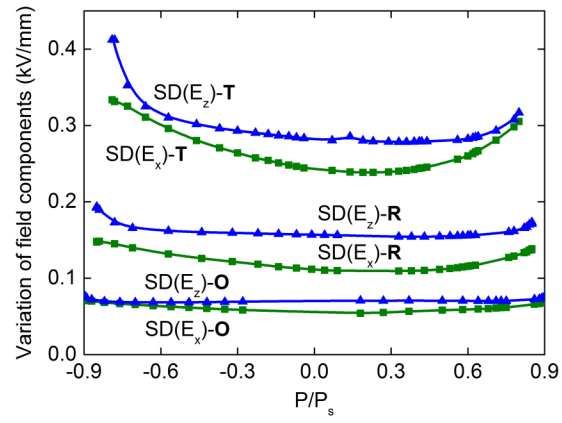

FIG. 6. Evolution of spatial field fluctuations presented by standard deviations of field components E_x and E_z in units of kV/mm during the polarization reversal in tetragonal (T), rhombohedral (R), and orthorhombic (O) systems.

when polarization changes. For all symmetries, variance of the E_z component exceeds that of the E_x component, the largest difference between them being observed in the initial polarization state ($-P_{\max}$) of the tetragonal ceramic.

C. Statistical field distributions

Evolution of the statistical field distributions during the polarization reversal exhibits nontrivial features which were not previously observed in 2D simulations [45]. As is seen in Fig. 7(a), the field distribution in the tetragonal ceramic is wide at the very beginning ($P/P_s = -0.81$). Then it rapidly becomes much narrower and higher when the total polarization changes up to $P/P_s = -0.662$ that takes a few tenth of millisecond on the timescale in Fig 3. After that the distribution height further slightly increases up to the polarization $P/P_s = -0.036$ and subsequently does not change up to $P/P_s = 0.634$. At the final stage, the distribution height decreases a little bit when the polarization grows to $P/P_s = 0.80$ virtually coinciding finally with that at $P/P_s = -0.662$.

Evolution of the field distribution in the rhombohedral ceramic exhibits partly similar but also some distinct features [Fig. 7(b)]. It transforms also rapidly from a wider to a narrower distribution when the polarization changes from $P/P_s = -0.851$ up to $P/P_s = -0.709$ that takes a few microseconds on the timescale in Fig 3. After that, however, it starts to decrease in height gradually changing its shape from a one-peak to a bimodal form when the polarization further changes to $P/P_s = -0.071$. Subsequently the distribution does not change essentially up to $P/P_s = 0.626$. At the final stage, the distribution height increases again when the polarization grows to $P/P_s = 0.848$ while the final distribution shape almost reproduces that in the state with $P/P_s = -0.709$.

The field distribution in the orthorhombic ceramic exhibits features similar to but not identical with the rhombohedral one. It transforms also rapidly from a wider initial one-peak distribution at $P/P_s = -0.902$ to a narrower distribution at $P/P_s = -0.704$ that takes a few microseconds on the timescale in Fig 3. After that it gradually decreases in

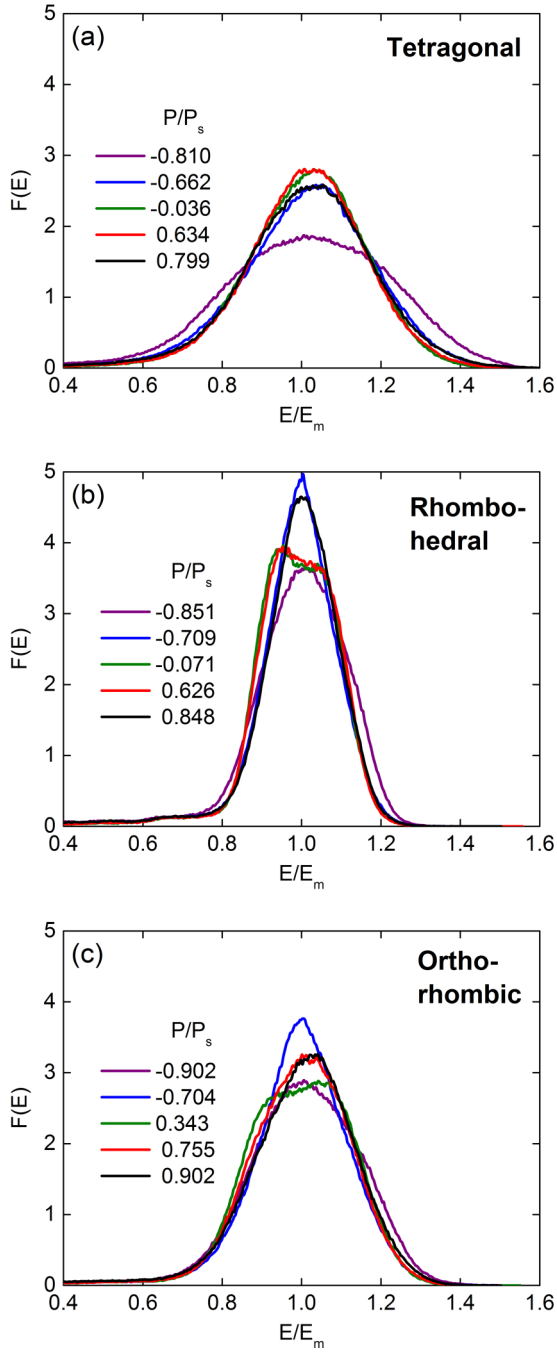

FIG. 7. Evolution of the statistical field distributions $F(E/E_m)$, where E_m is an applied field, in (a) tetragonal, (b) rhombohedral, and (c) orthorhombic ceramics for polarization variation from its negative to its positive maximum value. Representative polarization values are indicated in plots.

height changing its shape from a one-peak to a bimodal form when the polarization further changes to $P/P_s = 0.343$. Then the distribution height gradually increases again restoring a one-peak form when the polarization grows to $P/P_s = 0.755$ and remains stabilized until the end of the process at $P/P_s = 0.902$.

Notably, the saturated polarization values never reach the theoretical maximum magnitudes listed in Table I because the latter do not take into account possible disadvantageous local polarization configurations. Strong local depolarization fields appearing at such locations prevent reaching the maximum local polarizations thus limiting the total polarization value.

The evolution of the statistical distributions of fields seems to be more affected by statistical distributions of polarization directions $f(\theta, \varphi)$, which are narrower in the rhombohedral and orthorhombic ceramics, than by anisotropy of the permittivity tensor, which is substantially higher in the tetragonal and orthorhombic ceramics. This anisotropy, however, seems to be reflected by wider field distributions in the latter two systems. The absence of bimodal features in the field distribution of the tetragonal ceramic, Fig. 7(a), may also be due to the dominating role of the stray fields resulting from the highest anisotropy of this compound.

A general feature of evolution of statistical field distributions in all systems is that their shapes (particularly their widths) do not essentially change over the major part of the switching time (more than five decades). This behavior is in contrast to observations made in 2D simulations [45] where the statistical distribution was consistently broadening during the whole polarization reversal process. The difference to the simulation results of the 2D model [45] seems to stem from the stronger depression of the charge-induced depolarization fields by the assumed uniform reduction of polarization in the latter model, on the one hand, and from the overestimation of stray fields in 2D geometry, on the other hand.

The nonmonotonic variation of distributions with time may be rationalized as follows. In spite of the depolarization field reduction by different physical mechanisms in the actual model (see Sec. III B), the magnitude of these fields remains large and has a great impact on statistical field distributions in addition to the spatial fluctuations of the applied field due to the nonuniform granular structure of the system. On the one hand, the magnitude of spatial fluctuations of the depolarization fields generated by local bound charges roughly scales with the total polarization P. Thus, the variance of these fields is expected to be at maximum for the maximum values of polarization of either sign, the tendency observed in Fig. 6. On the other hand, the feedback through the depolarization fields provides an increasing synchronization of polarization switching in adjacent grains during the polarization reversal, which in turn leads to a continuous reduction of the variance of the depolarization fields with time. This makes the final distribution narrower than the initial one. Note, however, that, as soon as the voltage polarity is changed again, the distributions immediately transform back to the initial shapes as it should be in the completely symmetrical state. The difference in the behavior between tetragonal and rhombohedral ceramics might originate from much stronger anisotropy of the permittivity in the former. This means a stronger contribution of spatial field fluctuations of the applied field not related to the local charges. This dominating mechanism of the distribution broadening might hide in Fig. 7(a) the bimodal contribution from the depolarization fields which arises due to the cutoff of the high fields of the polarization charges. The behavior of field distributions in the orthorhombic ceramic bears features of both tetragonal and rhombohedral systems being in between them in anisotropy.

D. Spatial correlations

Two-point correlation functions of polarization and electric field components characterize how coherent the spatial fluctuations of these physical quantities are. The correlation coefficients are defined as

$$R_{E_\alpha,E_\beta}(\boldsymbol{\rho}) = \frac{\langle [E_\alpha(\mathbf{r}+\boldsymbol{\rho}) - \langle E_\alpha\rangle][E_\beta(\mathbf{r}) - \langle E_\beta\rangle]\rangle}{SD(E_\alpha)SD(E_\beta)}, \quad (13)$$

$$R_{p_\alpha,p_\beta}(\boldsymbol{\rho}) = \frac{\langle [p_\alpha(\mathbf{r}+\boldsymbol{\rho}) - \langle p_\alpha\rangle][p_\beta(\mathbf{r}) - \langle p_\beta\rangle]\rangle}{SD(p_\alpha)SD(p_\beta)}, \quad (14)$$

where α and β adopt values x, y, or z, and imply averaging over all pairs of points in the computational domain separated by a position vector $\boldsymbol{\rho}$. Due to cylindrical symmetry of the macroscopic system the correlation coefficients may only be dependent on the distance ρ and the angle the vector $\boldsymbol{\rho}$ makes with the field direction. For convenience, these coefficients will be displayed as polar diagrams in an arbitrary plain (ρ, ϕ) including the (vertical) field direction at $\phi = \pi/2$. A color legend from deep blue to deep red corresponds to the value variation from 0 to 1.

All cross correlations between the involved quantities including those between different polarization or field components were found to be negligible within the available accuracy. The autocorrelation coefficients of the polarization and field components exhibit nontrivial and distinct variations in compounds of different symmetries during the polarization reversal. This can only be captured when tracing a detailed evolution of the respective correlation functions. Since this analysis involves dozens of polar diagrams it is thoroughly presented in the Supplemental Material [70]. Here we merely show, for materials of different phase symmetries, exemplary plots of R_{E_z,E_z} and R_{p_z,p_z} coefficients in polarization states where correlations are most pronounced and anisotropic (Fig. 8). These demonstrate remarkable angle dependencies of correlations of both polarization and field components and an essential impact of the phase symmetry.

In all systems the correlations of the E_z component of the electric field are most pronounced in the x direction ($\phi = 0$ or $\phi = \pi$) as is seen in Figs. 8(a), 8(c) and 8(e) and in Figs. S1(f)–S1(j), S2(f)–S2(j), and S3(f)–S3(j) of the Supplemental Material [70]. Similarly, the correlations of the E_x component of the electric field are most pronounced in the z direction ($\phi = \pi/2$ or $\phi = 3\pi/2$) as is seen in Figs. S1(a)–S1(e), S2(a)–S2(e), and S3(a)–S3(e) of the Supplemental Material [70]. These correlations are apparently related to the continuity of the respective tangential field components across the cubic grain faces providing high field correlations at least in the neighbor grains. Beyond these features defined by the considered model geometry of the regular cubic grain array there are remarkable differences in the diagrams determined by the crystalline symmetries of different phases.

Differently from the field component correlations the correlation coefficient R_{p_x,p_x} reveals substantial variation between zero polarization state $P = 0$ and the maximum polarization states $P = \pm P_{\max}$ and also nontrivial anisotropic correlations in the intermediate states. In the tetragonal system, R_{p_x,p_x} is mostly of a fourfold symmetry with exception of the states around $P = 0$ where it becomes almost isotropic

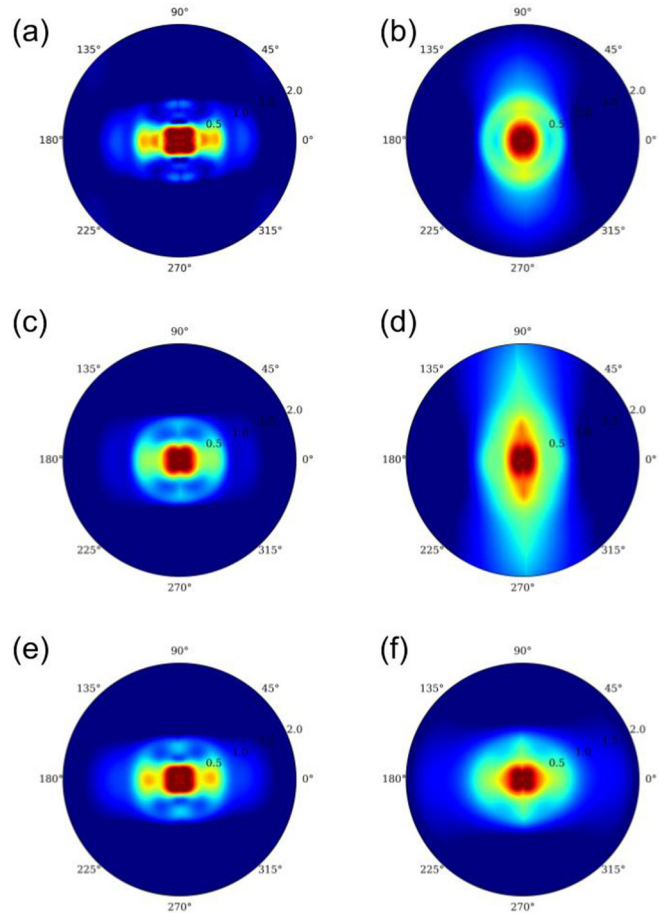

FIG. 8. Correlation coefficients R_{E_z,E_z} [(a), (c), and (e)] and R_{p_z,p_z} [(b), (d), and (f)] for tetragonal [at $P/P_s = 0.762$ (a) and -0.531 (b), respectively], rhombohedral [at $P/P_s = 0.853$ (c) and -0.299 (d), respectively], and orthorhombic [at $P/P_s = 0.895$ (e) and -0.548 (f), respectively] ceramics.

(Figs. S1(k)–S1(o) of the Supplemental Material [70]). In the rhombohedral system, R_{p_x,p_x} becomes additionally almost isotropic in the maximum polarization states $P = \pm P_{\max}$ revealing a twofold symmetry at intermediate polarization values (Figs. S2(k)–S2(o) of the Supplemental Material [70]). In the orthorhombic system, this coefficient retains a comparable fourfold symmetry at all polarization stages.

In contrast, the correlation coefficient R_{p_z,p_z} exhibits the strongest correlations along the z direction for the intermediate negative polarization values being otherwise virtually isotropic in the tetragonal system (Figs. S1(p)–S1(t) of the Supplemental Material [70]). These correlations along the poling direction are most strongly pronounced for intermediate negative to zero polarization values in the rhombohedral system (Figs. S2(p)–S2(t) of the Supplemental Material [70]). They are, however, only weakly visible in the orthorhombic system (Figs. S3(p)–S3(t) of the Supplemental Material [70]). The strongest z correlations in the rhombohedral ceramic result from the combination of the least anisotropic dielectric tensor of all systems considered and the relatively focused polarization axes distribution in this material (see Fig. 2).

With all anisotropic features and nonmonotonic behavior the correlations of both polarization and field remain short

range at the typical distance to the neighbor grain; a feature already observed in 2D simulations [45].

V. CONCLUSIONS

A long-standing question in the problem of polarization reversal kinetics was (i) why this process could be successfully described in statistical models [6–8] as statistically independent polarization-switching region by region as if the electric and elastic interactions of different regions were negligible. Furthermore, considering the evolution of depolarization fields in the course of polarization reversal [38–40,45], the question (ii) arises why the whole reversal process over many decades in time can be described as if the statistical distribution of the local fields does not change [10,12,15–17,25]. The presented simulations using the 3D-SMS model shed some light onto these problems.

Analysis of polarization and field correlations in Sec. IV D revealed that the depolarization field-mediated correlations remain short range at the typical scale of the grain size at all polarization stages for all phase symmetries considered. This means that, electrically, only nearest neighbors have effect on the polarization-switching process in a grain. Physical background of the short-range correlations is an effective screening of depolarization fields by adapting surface charges at grain boundaries [45]. This may answer the question (i) why statistical models [6–8] satisfactorily describe time dependence of the total polarization. On the other hand, the medium-range [33–35] correlations observed in ferroelectric ceramics and long-range [31,32] correlations observed in ferroelectric thin films seem rather to result from elastic interactions which cannot be screened as electrical ones.

The problem (ii) of emerging and varying depolarization field reveals different features in thin-film and bulk ferroelectrics. Being solely due to the presence of a very thin nonferroelectric layer below an electrode in the thin-film case [38,44,71] the depolarization field of this nature can hardly be significant in bulk ferroelectrics. In the latter case, a uniform depolarization field evolving together with the total polarization was conceived in Refs. [39,40]. From our point of view, in an experiment on the dc field-driven polarization reversal, such a field should be exactly compensated by charges at electrodes maintaining a constant voltage and thus would not play a role in polarization kinetics. On the other hand, spatial fluctuations of depolarization fields due to varying polarization of grains might be important. These fields arising due to mismatching polarizations in neighbor grains are typically much higher than coercive fields of ferroelectric materials. Therefore they are effectively reduced inside the grains by various physical mechanisms such as splitting in domains and semiconductor effects including band bending and possible accumulation of charged defects in surface states on grain boundaries. Since these mechanisms prevail during the whole polarization reversal process the statistical field distributions do not change much as was established in Sec. IV C. This explains why the NLS model [7,8,14,22] and the IFM model [12,15–17] neglecting the feedback due to depolarization fields are nevertheless able to describe the total polarization development in ferroelectric ceramics with high accuracy. We note that the statement on a stable statistical distribution of local electric fields resulting from the actual study using the 3D-SMS model revises the previous analysis based on the 2D-SMS model [45] where a broadening of the statistical field distribution during the polarization reversal was found. The physical reason of this discrepancy may be in overestimation of stray fields in 2D simulations as well as a simpler mechanism of the local field limitation assumed in the 2D-SMS model.

In conclusion, simulations using the 3D-SMS model helped to comprehend the paradoxically good performance of the statistical NLS and IFM models neglecting both the correlations between different switching regions and the feedback through the developing depolarization field. The 3D-SMS model itself, however, still provides only a fair agreement between the simulated time-dependent polarization reversal and available experimental data. Its most essential drawbacks are (i) the absence of possible polarization rotation in grains, which might strongly affect the switching kinetics, and (ii) the missing random shape of grains which could have a great effect on anisotropy of field and polarization correlations. Furthermore, since the local polarization development within grains is described by the statistical KAI approach, this model can hardly be applied to ceramics with a submicron grain size where a true single-domain state is expected to occur.

ACKNOWLEDGMENTS

Useful discussions with Jan Schultheiß , Jurij Koruza, and Andreas Klein are appreciated. R.K. gratefully acknowledges support of the research funded by Deutsche Forschungsgemeinschaft (GE 1171/7-1).

APPENDIX A: DIRECTIONAL STATISTICS OF POLARIZATIONS IN HIGHLY POLED UNCORRELATED FERROELECTRIC CERAMICS OF RHOMBOHEDRAL SYMMETRY

The distribution function of possible polarization directions in a polycrystalline ferroelectric of rhombohedral symmetry compatible with a given strong field direction can be derived in the spirit of the approach by Uchida and Ikeda [49], as was earlier done for the ceramics of tetragonal symmetry [48]. In their original work [49], Uchida and Ikeda avoided derivation of the distribution of polarization orientations around the applied field and used an alternative way to evaluate the mean directional cosine between the polarization and the applied field. To this end they fixed the polarization direction of a ferroelectric cell and averaged the directional cosine of the field over all possible field directions compatible with the chosen polarization direction. It was assumed that the crystal lattice orientation is arbitrary and completely decoupled from the form and orientation of grains.

Introducing the Cartesian coordinates aligned with a pseudocubic cell [see Fig. 9(a)] it is sufficient for the case of rhombohedral symmetry to consider a solid angle $0<\varphi<\pi/4$, $0<\vartheta<\pi/4$, in terms of a conventionally associated spherical coordinate system (r,φ,ϑ), comprising one of eight possible polarization directions with a Cartesian unit vector $\nu=(1,1,1)/\sqrt{3}$. Any field direction indicated by a unit vector $\mathbf{n}=(\sin\vartheta\cos\varphi,\sin\vartheta\sin\varphi,\cos\vartheta)$ from the considered

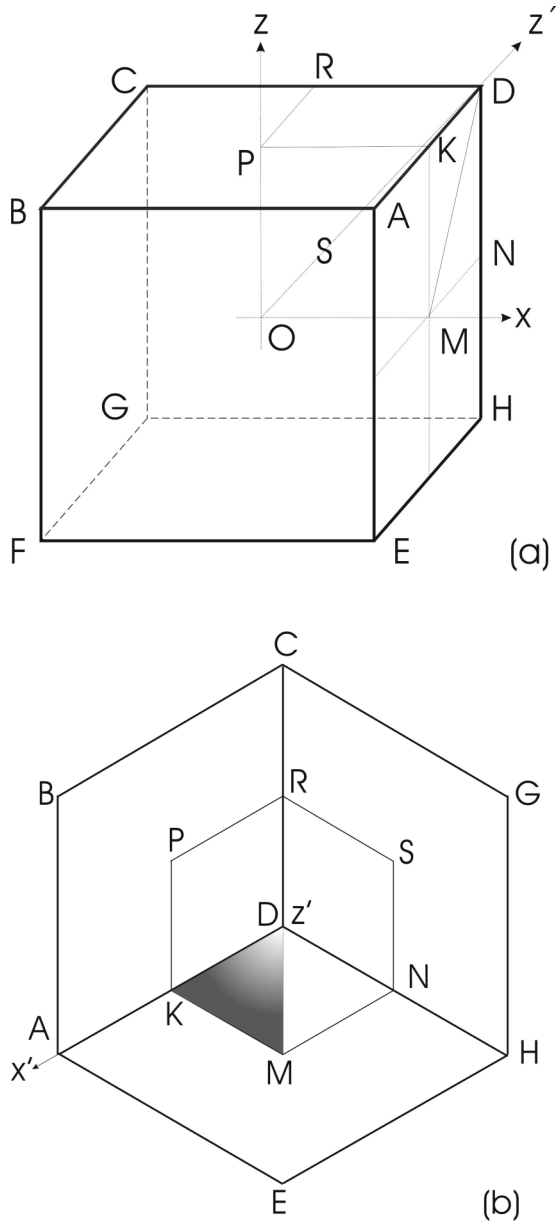

FIG. 9. (a) Scheme of a pseudocubic cell disclosing a polarization in the positive z' direction and a solid angle $OPRSNMK$ of strong electric field directions compatible with this polarization orientation. (b) Two-dimensional projection of the pseudocubic cell seen from a remote point at the axis z'. Shaded area DKM determines the considered solid angle with the center at origin.

solid angle, comprising directions crossing the origin O and the cube faces $DKPR$, $DRSN$, $DNMK$ in Fig. 9, equally favors the selected polarization direction ν. Crossing the border of the solid angle $PRSNMK$ by the field direction results in a 70.5°-polarization rotation to one of the neighboring stable polarization directions, OA, OC, OH.

The probability density for the field directions is uniform with a distribution function $p_r(\vartheta, \varphi) = 2/\pi$, the reciprocal value of the comprised solid angle of $4\pi/8 = \pi/2$, but it retains anisotropy through the choice of the considered solid angle. By averaging of a direction cosine $\cos\alpha = (\mathbf{n} \cdot \nu)$ with a tilt angle α over the chosen solid angle using the distribution function $p_r(\vartheta, \varphi)$ the mean projection of the field on the selected polarization direction can be evaluated:

$$\langle \cos\alpha \rangle = \int_0^{\pi/2} d\varphi \int_0^{\pi/2} d\vartheta \; p_r(\vartheta, \varphi) \sin\vartheta \cos\alpha = 0.866, \tag{A1}$$

which coincides with the result by Uchida and Ikeda [49] and also equals the mean polarization projection from the directions compatible with the fixed field direction.

To derive the distribution function of possible polarization directions compatible with a given field direction we chose the latter along the vector ν and rotate the Cartesian coordinate system (x, y, z) so that a new axis z' also coincides with ν (see Fig. 9). Basis unit vectors of the new Cartesian coordinate system (x', y', z') expressed in terms of the old one read $\mathbf{n}_{x'} = (1, -2, 1)/\sqrt{6}$, $\mathbf{n}_{y'} = (1, 0, 1)/\sqrt{2}$, and $\mathbf{n}_{z'} = (1, 1, 1)/\sqrt{3}$. Observed from a remote point at the axis z' the cubic cell looks like a figure of a sixfold rotational symmetry (being in fact threefold) where x' axis is hidden behind the line DA [Fig. 9(b)]. In terms of a spherical coordinate system (r, ϕ, θ) conventionally associated with the Cartesian system (x', y', z') it is sufficient to consider the azimuthal angle region between the directions $\phi = 0$ (hidden behind the line DA) and $\phi = \pi/3$ (hidden behind the line DE). The distribution function of interest $f_r(\theta, \phi)$ must be ϕ independent since due to arbitrary crystal orientation in different grains there is no selected direction in the (x', y') plane normal to the applied field. Therefore it can be derived by averaging over the azimuthal angle from the relation

$$2\pi \sin\theta \, d\theta \; f_r(\theta, \phi) = 6 \int_{\phi_0}^{\pi/3} d\phi' \; \sin\theta \, d\theta \; p_r(\theta, \phi'). \tag{A2}$$

The lower integration limit ϕ_0 is defined by the line KM bounding the solid angle $ODKM$. For any unit vector $\mathbf{n} = (\sin\theta\cos\phi, \sin\theta\sin\phi, \cos\theta)$ crossing this line a condition $\varphi = 0$ applies, therefore the relations

$$\begin{aligned} (\mathbf{n} \cdot \mathbf{n}_{z'}) &= \cos\theta = (\sin\vartheta + \cos\vartheta)/\sqrt{3}, \\ (\mathbf{n} \cdot \mathbf{n}_{x'}) &= \sin\theta\cos\phi = (\sin\vartheta + \cos\vartheta)/\sqrt{6} \end{aligned} \tag{A3}$$

are valid. By dividing the second equation by the first one a relation $\tan\theta\cos\phi = 1/\sqrt{2}$ results which can be alternatively resolved as

$$\theta_r(\phi) = \arctan\left(\frac{1}{\sqrt{2}\cos\phi}\right) \quad \text{or} \quad \phi_r(\theta) = \arccos\left(\frac{\cot\theta}{\sqrt{2}}\right). \tag{A4}$$

When ϕ varies from 0 to $\pi/3$ the function θ_r monotonically rises from $\theta_{r1} = \arctan(1/\sqrt{2})$ (corresponding to 35.2°) to $\theta_{r2} = \arctan\sqrt{2}$ (corresponding to 54.7°). As long as $\theta < \theta_{r1}$ integration in Eq. (A2) goes from $\phi_0 = 0$ to $\pi/3$ which results in a constant value of $f_r(\theta, \phi)$. When $\theta_{r1} < \theta < \theta_{r2}$ integration in Eq. (A2) goes from $\phi_0 = \phi_r$ to $\pi/3$ which results finally in a directional distribution

$$f_r(\theta, \phi) = \begin{cases} \frac{2}{\pi}, & 0 \leqslant \theta \leqslant \theta_{r1}, \\ \frac{6}{\pi^2}\left[\frac{\pi}{3} - \arccos\left(\frac{\cot\theta}{\sqrt{2}}\right)\right], & \theta_{r1} \leqslant \theta \leqslant \theta_{r2}, \end{cases} \tag{A5}$$

which is properly normalized to unity when integrating over the full solid angle. Averaging using Eq. (A5) brings about mean values $\langle \cos\theta \rangle = 0.866$ and $\langle \cos^2\theta \rangle = 0.758$ in agreement with Uchida and Ikeda [49].

APPENDIX B: DIRECTIONAL STATISTICS OF POLARIZATIONS IN HIGHLY POLED UNCORRELATED FERROELECTRIC CERAMICS OF ORTHORHOMBIC SYMMETRY

Orthorhombic symmetry allows twelve stable polarization directions, namely, four in-plane diagonal orientations in each of (x, y), (y, z), and (x, z) planes in the Cartesian coordinates (x, y, z) aligned with a pseudocubic cell [see Fig. 10(a)].

Similar to the case of rhombohedral symmetry we start with determination of a solid angle comprising possible strong field directions compatible with a certain polarization direction, in this case exemplarily given by a unit vector $\nu = (1, 1, 0)/\sqrt{2}$. This polarization is compatible with a strong electric field applied in any direction crossing the origin O and a rhombic area $ATBS$ (Fig. 10). Crossing the border of this area by the field direction would entail 60° switching of the polarization to one of the neighboring stable polarization directions given by vectors OL, OM, ON, OP [Fig. 10(a)]. The solid angle $OATBS$ has a fourfold symmetry so that it is sufficient to consider one quarter of it bounded by the triangle BKT. The lines KT and KB are defined, respectively, by conditions $0 < \varphi < \pi/4$, $\vartheta = \pi/2$ and $\varphi = \pi/4$, $\pi/2 < \vartheta < \pi/2 + \theta_o$ with $\theta_o = \arctan(1/\sqrt{2})$ in terms of a conventionally associated spherical coordinate system (r, φ, ϑ). The boundary BT is determined by a unit vector directed to this line from origin O, $\mathbf{n}_0 = (\sqrt{\sin^2\vartheta - \cos^2\vartheta}, -\cos\vartheta, \cos\vartheta)$, and obeys a relation $\tan\vartheta = -1/\sin\varphi$ or $\vartheta_0(\varphi) = \pi - \arctan(1/\sin\varphi)$.

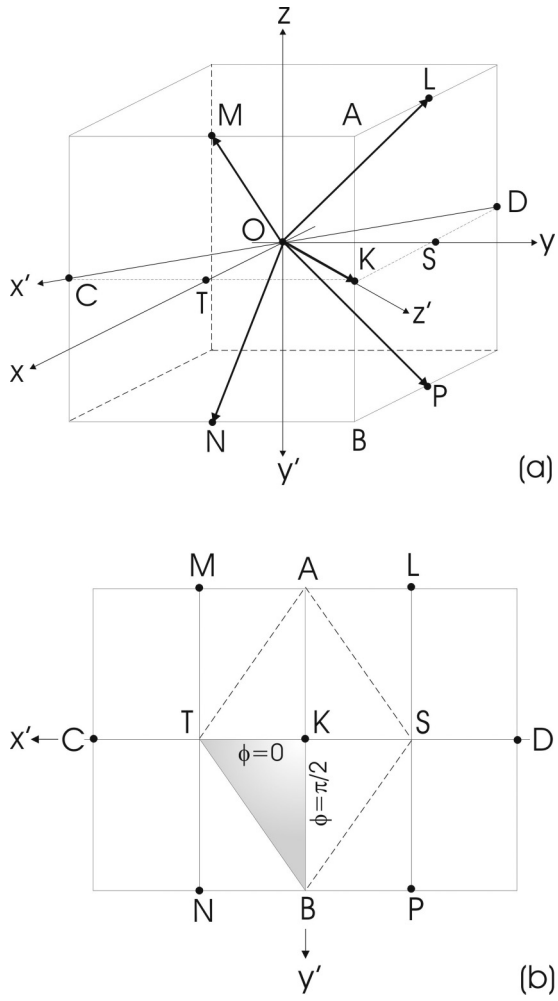

FIG. 10. (a) Scheme of a pseudocubic cell disclosing a polarization in the positive z' direction and a solid angle $OATBS$ of strong electric field directions compatible with this polarization orientation. (b) Two-dimensional projection of the pseudocubic cell seen from a remote point at the axis z'. Shaded area BKT determines the considered solid angle with the center at origin.

By integrating over the solid angle $OATBS$ its value is found to equal $\pi/3$ as it should be considering the 12 available polarization directions over the total solid angle. Since all field directions with the solid angle $OATBS$ are equally in favor of the polarization direction ν the probability density for the field directions is uniform with a distribution function $p_o(\vartheta, \varphi) = 3/\pi$, the reciprocal value of the comprised solid angle. By averaging of a direction cosine $\cos\alpha = (\mathbf{n} \cdot \nu)$ with a tilt angle α of an arbitrary field direction $\mathbf{n}$ over the chosen solid angle the mean projection of the field on the selected polarization direction can be evaluated using the distribution function $p_o(\vartheta, \varphi)$:

$$\langle \cos\alpha \rangle = 4 \int_0^{\pi/4} d\varphi \int_{\pi/2}^{\vartheta_0(\varphi)} d\vartheta \; p_o(\vartheta, \varphi) \sin\vartheta \cos\alpha = 0.912, \tag{B1}$$

a value known from literature [52,53].

To derive the distribution function of possible polarization directions compatible with a given field direction we chose the latter along the vector ν and rotate the Cartesian coordinate system (x, y, z) so that a new axis z' also coincides with ν [see Fig. 10(a)]. Basis unit vectors of the new Cartesian coordinate system (x', y', z') expressed in terms of the old one read $\mathbf{n}_{x'} = (1, -1, 0)/\sqrt{2}$, $\mathbf{n}_{y'} = (0, 0, -1)$, and $\mathbf{n}_{z'} = (1, 1, 0)/\sqrt{2}$. Observed from a remote point at the axis z' the cubic cell looks like a rectangle with the rhombic boundary of the considered solid angle $ASBT$ [Fig. 10(b)]. In terms of a spherical coordinate system (r, ϕ, θ) conventionally associated with the Cartesian system (x', y', z') it is sufficient to consider a quarter of the above solid angle delineated by the triangle BKT [shadowed area in Fig. 10(b)] within the azimuthal angle region between $\phi = 0$ (line KT) and $\phi = \pi/2$ (line KB). An equation describing the last line bounding the solid angle BT can be derived from the relations

$$\begin{aligned}
(\mathbf{n}_0 \cdot \mathbf{n}_{z'}) &= \cos\theta = \frac{\sqrt{\sin^2\vartheta - \cos^2\vartheta} - \cos\vartheta}{\sqrt{2}}, \\
(\mathbf{n}_0 \cdot \mathbf{n}_{x'}) &= \sin\theta\cos\phi = \frac{\sqrt{\sin^2\vartheta - \cos^2\vartheta} + \cos\vartheta}{\sqrt{2}}, \\
(\mathbf{n}_0 \cdot \mathbf{n}_{y'}) &= \sin\theta\sin\phi = -\cos\vartheta,
\end{aligned} \tag{B2}$$

from which an equation

$$\cos(\phi - \phi_0) = 1/\sqrt{3}\tan\theta \tag{B3}$$

with $\phi_0 = \arctan\sqrt{2}$ results.

The distribution function of possible polarization directions in a polycrystalline ferroelectric orthorhombic symmetry compatible with a given strong field direction $f_o(\theta, \phi)$ must be ϕ independent since due to arbitrary crystal orientation in different grains there is no selected direction in the (x', y') plane normal to the applied field. Therefore it can be derived by averaging over the azimuthal angle from the relation

$$2\pi \sin\theta\, d\theta\; f_o(\theta, \phi) = 4\int d\phi'\, \sin\theta\, d\theta\; p_o(\theta, \phi'), \tag{B4}$$

which looks similar to Eq. (A2) however covers a more complicated integration region. According to Eq. (B3), in the polar angle region $0 < \theta < \pi/6$ integration in Eq. (B4) goes over the azimuthal region $0 < \phi' < \pi/2$. In the polar angle region $\pi/6 < \theta < \theta_o$ integration over the azimuthal angle includes two regions $0 < \phi' < \phi_-$ and $\phi_+ < \phi' < \pi/2$ with $\phi_\pm = \phi_0 \pm \arccos(1/\sqrt{3}\tan\theta)$ being the solutions to Eq. (B3). And finally in the polar angle region $\theta_o < \theta < \pi/4$ integration over the azimuthal angle goes over the region $0 < \phi' < \phi_-$ only (the other region disappears). This leads to the directional distribution

$$f_o(\theta, \phi) = \begin{cases} \frac{3}{\pi}, & 0 \leqslant \theta \leqslant \pi/6, \\ \frac{6}{\pi^2}\left[\frac{\pi}{2} - 2\arccos\left(\frac{\cot\theta}{\sqrt{3}}\right)\right], & \pi/6 \leqslant \theta \leqslant \theta_o, \\ \frac{6}{\pi^2}\left[\phi_0 - \arccos\left(\frac{\cot\theta}{\sqrt{3}}\right)\right], & \theta_o \leqslant \theta \leqslant \pi/4, \end{cases} \tag{B5}$$

which is properly normalized to unity. Averaging using Eq. (B5) brings about mean values $\langle\cos\theta\rangle = 0.912$ and $\langle\cos^2\theta\rangle = 0.835$ confirming Refs. [52,53].

APPENDIX C: SPATIAL FLUCTUATIONS OF BOUND CHARGES IN HIGHLY POLED, UNCORRELATED FERROELECTRIC CERAMICS

Variances of the surface bound charge densities at the differently oriented grain boundaries are defined by coefficients

$$a = \langle\cos(\theta_{n,k,m})^2\rangle \quad \text{and} \quad b = \langle\cos(\theta_{n,k,m})\rangle^2. \tag{C1}$$

Using the distribution functions derived in Appendixes A and B and Ref. [48] they can be calculated to equal $a_t = 0.701$ and $b_t = 0.691$ for the tetragonal case, $a_r = 0.758$ and $b_r = 0.75$ for the rhombohedral case, and $a_o = 0.835$ and $b_o = 0.832$ for the orthorhombic case.

Thanks to statistical independence of the polarization directions in neighbor grains the variance of the charge density at the grain boundaries normal to the axis z [Eq. (6)] is reduced to

$$\left\langle\left(\sigma^z_{n,k,m}\right)^2\right\rangle = 2P_s^2(a - b). \tag{C2}$$

The variances of the charge densities at the grain boundaries perpendicular to the axes x [Eq. (7)] and y [Eq. (8)] are defined by

$$\left\langle\left(\sigma^x_{n,k,m}\right)^2\right\rangle = \left\langle\left(\sigma^y_{n,k,m}\right)^2\right\rangle = P_s^2(1 - a). \tag{C3}$$

These result in standard deviations of the respective charge densities [Eq. (9)] listed in Table I for different phase symmetries.

For calculation of various physical quantities, for example, of the field component variances [48], the knowledge of correlation functions of charge densities is needed. They appear to be diagonal in Cartesian indices β, β' and involve only the identical and the next neighbor indexes n, k, m:

$$\begin{aligned} \left\langle\sigma^x_{n,k,m}\sigma^x_{n',k',m'}\right\rangle &= \left(P_s^2/2\right)(1 - a)\delta_{k,k'}\delta_{m,m'} \\ &\quad \times (2\delta_{n,n'} - \delta_{n,n'-1} - \delta_{n,n'+1}), \\ \left\langle\sigma^y_{n,k,m}\sigma^y_{n',k',m'}\right\rangle &= \left(P_s^2/2\right)(1 - a)\delta_{n,n'}\delta_{m,m'} \\ &\quad \times (2\delta_{k,k'} - \delta_{k,k'-1} - \delta_{k,k'+1}), \\ \left\langle\sigma^z_{n,k,m}\sigma^z_{n',k',m'}\right\rangle &= P_s^2(a - b)\delta_{n,n'}\delta_{k,k'} \\ &\quad \times (2\delta_{m,m'} - \delta_{m,m'-1} - \delta_{m,m'+1}). \end{aligned} \tag{C4}$$

[1] J. F. Scott, *Ferroelectric Memories* (Springer, Berlin, 2000).
[2] R. Landauer, J. Appl. Phys. **28**, 227 (1957).
[3] R. C. Miller and G. Weinreich, Phys. Rev. **117**, 1460 (1960).
[4] A. Kolmogoroff, Izv. Akad. Nauk SSSR, Ser. Math. **1**, 355 (1937).
[5] M. Avrami, J. Chem. Phys. **8**, 212 (1940).
[6] Y. Ishibashi and Y. Takagi, J. Phys. Soc. Jpn. **31**, 506 (1971).
[7] A. K. Tagantsev, I. Stolichnov, N. Setter, J. S. Cross, and M. Tsukada, Phys. Rev. B **66**, 214109 (2002).
[8] J. Y. Jo, H. S. Han, J.-G. Yoon, T. K. Song, S.-H. Kim, and T. W. Noh, Phys. Rev. Lett. **99**, 267602 (2007).
[9] S. Zhukov, S. Fedosov, J. Glaum, T. Granzow, Y. A. Genenko, and H. von Seggern, J. Appl. Phys. **108**, 014105 (2010).
[10] S. Zhukov, Y. A. Genenko, O. Hirsch, J. Glaum, T. Granzow, and H. von Seggern, Phys. Rev. B **82**, 014109 (2010).
[11] D. Kedzierski, E. V. Kirichenko, and V. A. Stephanovich, Phys. Lett. A **375**, 685 (2011).
[12] Y. A. Genenko, S. Zhukov, S. V. Yampolskii, J. Schütrumpf, R. Dittmer, W. Jo, H. Kungl, M. J. Hoffmann, and H. von Seggern, Adv. Funct. Mater. **22**, 2058 (2012).
[13] Y. A. Genenko, R. Khachaturyan, J. Schultheiß, A. Ossipov, J. E. Daniels, and J. Koruza, Phys. Rev. B **97**, 144101 (2018).
[14] J. Y. Jo, S. M. Yang, H. S. Han, D. J. Kim, W. S. Choi, T. W. Noh, T. K. Song, J.-G. Yoon, C.-Y. Koo, J.-H. Cheon, and S.-H. Kim, Appl. Phys. Lett. **92**, 012917 (2008).
[15] S. Zhukov, Y. A. Genenko, M. Acosta, H. Humburg, W. Jo, J. Rödel, and H. von Seggern, Appl. Phys. Lett. **103**, 152904 (2013).
[16] S. Zhukov, H. Kungl, Y. A. Genenko, and H. von Seggern, J. Appl. Phys. **115**, 014103 (2014).

[17] S. Zhukov, M. Acosta, Y. A. Genenko, and H. von Seggern, J. Appl. Phys. **118**, 134104 (2015).

[18] S. Zhukov, Y. A. Genenko, J. Koruza, J. Schultheiß, H. von Seggern, W. Sakamoto, H. Ichikawa, T. Murata, K. Hayashi, and T. Yogo, Appl. Phys. Lett. **108**, 012907 (2016).

[19] S. Zhukov, J. Glaum, H. Kungl, E. Sapper, R. Dittmer, Y. A. Genenko, and H. von Seggern, J. Appl. Phys. **120**, 064103 (2016).

[20] R. Khachaturyan, S. Zhukov, J. Schultheiß, C. Galassi, C. Reimuth, J. Koruza, H. von Seggern, and Y. A. Genenko, J. Phys. D: Appl. Phys. **50**, 045303 (2017).

[21] J. Schütrumpf, S. Zhukov, Y. A. Genenko, and H. von Seggern, J. Phys. D: Appl. Phys. **45**, 165301 (2012).

[22] A. Nautiyal, K. C. Sekhar, N. P. Pathak, N. Dabra, J. S. Hundal, and R. Nath, Appl. Phys. A **99**, 941 (2010).

[23] N. Dabra, J. S. Hundal, A. Nautiyal, K. C. Sekhar, and R. Nath, J. Appl. Phys. **108**, 024108 (2010).

[24] D. Zhao, I. Katsouras, K. Asadi, P. W. M. Blom, and D. M. de Leeuw, Phys. Rev. B **92**, 214115 (2015).

[25] J. Lee, A. J. J. M. van Breemen, V. Khikhlovskyi, M. Kemerink, R. A. J. Janssen, and G. H. Gelinck, Sci. Rep. **6**, 24407 (2016).

[26] D. Zhao, I. Katsouras, K. Asadi, W. A. Groen, P. W. M. Blom, and D. M. de Leeuw, Appl. Phys. Lett. **108**, 232907 (2016).

[27] A. V. Gorbunov, T. Putzeys, I. Urbanavičiūtė, R. A. J. Janssen, M. Wübbenhorst, R. P. Sijbesma, and M. Kemerink, Phys. Chem. Chem. Phys. **18**, 23663 (2016).

[28] K. C. Sekhar, A. Nautiyal, and R. Nath, Appl. Phys. A **95**, 415 (2009).

[29] N. Mishra, N. Dabra, A. Nautiyal, J. S. Hundal, G. D. Varma, N. P. Pathak, and R. Nath, Ferroelectr. Lett. **42**, 75 (2015).

[30] I. Stolichnov, L. Malin, E. Colla, A. K. Tagantsev, and N. Setter, Appl. Phys. Lett. **86**, 012902 (2005).

[31] P. Bintachitt, S. Trolier-McKinstry, K. Seal, S. Jesse, and S. V. Kalinin, Appl. Phys. Lett. **94**, 042906 (2009).

[32] K. Seal, S. Jesse, M. P. Nikiforov, S. V. Kalinin, I. Fujii, P. Bintachitt, and S. Trolier-McKinstry, Phys. Rev. Lett. **103**, 057601 (2009).

[33] J. E. Daniels, M. Majkut, Q. Cao, S. Schmidt, J. Wright, W. Jo, and J. Oddershede, Sci. Rep. **6**, 22820 (2016).

[34] M. Majkut, J. E. Daniels, J. P. Wright, S. Schmidt, and J. Oddershede, J. Am. Ceram. Soc. **100**, 393 (2017).

[35] S. Mantri, J. Oddershede, D. Damjanovic, and J. E. Daniels, Acta Mater. **128**, 400 (2017).

[36] J. E. Zhou, T.-L. Cheng, and Y. U. Wang, J. Appl. Phys. **111**, 024105 (2012).

[37] A. Leschhorn and H. Kliem, J. Appl. Phys. **121**, 014103 (2017).

[38] X. J. Lou, J. Phys.: Condens. Matter **21**, 012207 (2009).

[39] G. Viola, K. B. Chong, F. Guiu, and M. J. Reece, J. Appl. Phys. **115**, 034106 (2014).

[40] K. Auluck and E. C. Kan, IEEE Trans. Electron Devices **63**, 631 (2016).

[41] D. M. Marincel, H. Zhang, A. Kumar, S. Jesse, S. V. Kalinin, W. M. Rainforth, I. M. Reaney, C. A. Randall, and S. Trolier-McKinstry, Adv. Funct. Mater. **24**, 1409 (2014).

[42] D. M. Marincel, H. R. Zhang, J. Britson, A. Belianinov, S. Jesse, S. V. Kalinin, L. Q. Chen, W. M. Rainforth, I. M. Reaney, C. A. Randall, and S. Trolier-McKinstry, Phys. Rev. B **91**, 134113 (2015).

[43] D. M. Marincel, H. Zhang, S. Jesse, A. Belianinov, M. B. Okatan, S. V. Kalinin, W. M. Rainforth, I. M. Reaney, C. A. Randall, and S. Trolier-McKinstry, J. Am. Ceram. Soc. **98**, 1848 (2015).

[44] Y. A. Genenko, J. Wehner, and H. von Seggern, J. Appl. Phys. **114**, 084101 (2013).

[45] R. Khachaturyan, J. Wehner, and Y. A. Genenko, Phys. Rev. B **96**, 054113 (2017).

[46] L. Padurariu, L. Curecheriu, C. Galassi, and L. Mitoseriu, Appl. Phys. Lett. **100**, 252905 (2012).

[47] L. Padurariu, L. Petronela Curecheriu, and L. Mitoseriu, Acta Mater. **103**, 724 (2016).

[48] Y. A. Genenko, J. Glaum, O. Hirsch, H. Kungl, M. J. Hoffmann, and T. Granzow, Phys. Rev. B **80**, 224109 (2009).

[49] N. Uchida and T. Ikeda, Jpn. J. Appl. Phys. **6**, 1079 (1967).

[50] R. E. Newnham, *Properties of Materials. Anisotropy, Symmetry, Structure* (Oxford University Press, Oxford, 2005).

[51] J. L. Jones, M. Hoffman, and K. J. Bowman, J. Appl. Phys. **98**, 024115 (2005).

[52] H. G. Baerwald, Phys. Rev. **105**, 480 (1957).

[53] B. Jaffe, W. R. Cook, Jr., and H. Jaffe, *Piezoelectric Ceramics* (Academic Press, New York, 1971).

[54] M. J. Haun, E. Furman, S. J. Jang, and L. E. Cross, Ferroelectrics **99**, 63 (1989).

[55] X.-H. Du, U. Belegundu, and K. Uchino, Jap. J. Appl. Phys. **36**, 5580 (1997).

[56] E. Wiesendanger, Ferroelectrics **6**, 263 (1974).

[57] L. Liang, Y. L. Li, L.-Q. Chen, S. Y. Hu, and G.-H. Lu, J. Appl. Phys. **106**, 104118 (2009).

[58] W. J. Merz, Phys. Rev. **95**, 690 (1954).

[59] D. C. Lupascu, S. Fedosov, C. Verdier, J. Rodel, and H. von Seggern, J. Appl. Phys. **95**, 1386 (2004).

[60] J. E. Daniels, C. Cozzan, S. Ukritnukun, G. Tutuncu, J. Andrieux, J. Glaum, C. Dosch, W. Jo, and J. L. Jones, J. Appl. Phys. **115**, 224104 (2014).

[61] S. Gorfman, H. Simons, T. Iamsasri, S. Prasertpalichat, D. P. Cann, H. Choe, U. Pietsch, Y. Watier, and J. L. Jones, Sci. Rep. **6**, 20829 (2016)

[62] C. M. Fancher, S. Brewer, C. C. Chung, S. Rohrig, T. Rojac, G. Esteves, M. Deluca, N. Bassiri-Gharb, and J. L. Jones, Acta Mater. **126**, 36 (2017).

[63] A. K. Tagantsev, L. E. Cross, and J. Fousek, *Domains in Ferroic Crystals and Thin Films* (Springer, Berlin, 2010).

[64] Y. Watanabe, Phys. Rev. B **57**, 789 (1998).

[65] M. Y. Gureev, A. K. Tagantsev, and N. Setter, Phys. Rev. B **83**, 184104 (2011).

[66] Y. A. Genenko, O. Hirsch, and P. Erhart, J. Appl. Phys. **115**, 104102 (2014).

[67] M. Blömker, E. Erdem, S. Li, S. Weber, A. Klein, J. Rödel, and T. Frömling, J. Am. Ceram. Soc. **99**, 543 (2016).

[68] J. H. Kim and C. S. Yoon, Appl. Phys. Lett. **81**, 3332 (2002).

[69] J. Schultheiß, L. Liu, H. Kungl, M. Weber, L. Kodumudi Venkataraman, S. Checchia, D. Damjanovic, J. E. Daniels, and J. Koruza, Acta Mater. **157**, 355 (2018).

[70] See Supplemental Material at http://link.aps.org/supplemental/10.1103/PhysRevB.98.134106 for polar diagrams of correlation coefficients for polarization and electric field components.

[71] A. K. Tagantsev and I. A. Stolichnov, Appl. Phys. Lett. **74**, 1326 (1999).